

Revisiting the large-scale CMB anomalies: The impact of the SZ signal from the Local Universe.

Gabriel Jung¹ *, Nabila Aghanim¹, Jenny Sorce^{2, 1, 3}, Benjamin Seidel⁴, Klaus Dolag^{4, 5}, Marian Douspis¹

¹ Université Paris-Saclay, CNRS, Institut d'Astrophysique Spatiale, 91405 Orsay, France

² Univ. Lille, CNRS, Centrale Lille, UMR 9189 CRISAL, 59000 Lille, France

³ Leibniz-Institut für Astrophysik (AIP), An der Sternwarte 16, 14482 Potsdam, Germany

⁴ Universitäts-Sternwarte, Fakultät für Physik, Ludwig-Maximilians Universität, Scheinerstr. 1, 81679 München, Germany

⁵ Max-Planck-Institut für Astrophysik, Karl-Schwarzschild-Straße 1, 85741 Garching, Germany

ABSTRACT

The full sky measurements of the Cosmic Microwave Background (CMB) temperature anisotropies by *WMAP* and *Planck* have highlighted the presence of several unexpected isotropy-breaking features on the largest angular scales.

In this work, we investigate the impact of the local large-scale structure on these anomalies through the thermal and kinetic Sunyaev-Zeldovich effects. We use a constrained hydrodynamical simulation that reproduces the local Universe in a box of $500 h^{-1}$ Mpc to construct full sky maps of the temperature anisotropies produced by these two CMB secondary effects and discuss their statistical properties on large angular scales. We show the significant role played by the Virgo cluster on these scales, and compare it to theoretical predictions and random patches of the universe obtained from the hydrodynamical simulation *Magneticum*.

We explore three of the main CMB large-scale anomalies—i.e., lack of correlation, quadrupole-octopole alignment and hemispherical asymmetry—, both in the latest *Planck* data (PR4), where they are detected at a similar level to the previous releases, and using the simulated secondaries from the local Universe, verifying their negligible impact.

1. Introduction

The high-precision observations of the CMB anisotropies of the last two decades have highlighted the Gaussian and isotropic nature of the early Universe over a wide range of scales, corresponding to a standard Λ CDM Universe with a period of inflation in its simplest models. However, on the largest angular scales, an ensemble of features (for recent reviews, see Schwarz et al. 2016; Abdalla et al. 2022) breaking this statistical isotropy or Gaussianity have been observed in the CMB temperature field of both *WMAP* and *Planck* (Planck Collaboration 2014b, 2016a, 2020a). This includes the lack of correlation anomaly (Hinshaw et al. 1996; Bennett et al. 2003; Spergel et al. 2003; Copi et al. 2007, 2009; Gruppuso 2014; Copi et al. 2015a), also formulated at a lack of power (Monteserin et al. 2008; Cruz et al. 2011; Gruppuso et al. 2013; Billi et al. 2019; Natale et al. 2019; Billi et al. 2023), the hemispherical asymmetry (Eriksen et al. 2004, 2007; Hansen et al. 2009; Hoftuft et al. 2009; Akrami et al. 2014; Adhikari 2015; Gimeno-Amo et al. 2023; Kester et al. 2023), the quadrupole-octopole alignment (de Oliveira-Costa et al. 2004; Schwarz et al. 2004; Land & Magueijo 2005; Gruppuso & Gorski 2010; Copi et al. 2015b; Marcos-Caballero & Martínez-González 2019; Patel et al. 2024) and the cold spot (Vielva et al. 2004; Cruz et al. 2005, 2006; Vielva 2010; Marcos-Caballero et al. 2017; Lambas et al. 2024). The occurrence of one of these so-called large-scale anomalies in CMB simulations of standard Λ CDM universes is rare, typically below the percent level, and even much lower when considered jointly, as they seem mostly statistically independent (Muir et al. 2018; Jones et al. 2023). Moreover, future observations of these large cosmological scales will improve the statistical significance of these anomalies, for example in the CMB polarisation field (see e.g., Dvorkin et al. 2008; Billi et al. 2019; Chiochetta et al. 2021;

Shi et al. 2023, including some analyses of the *Planck* polarisation data) with the satellite *LiteBIRD* (Suzuki et al. 2018) or in the Cosmological Gravitational Wave Background (Galloni et al. 2022, 2023) with *LISA* (Amaro-Seoane et al. 2017; Barausse et al. 2020), and help to probe if they are signatures of unknown physics.

Many such primordial signatures have been studied, recent works include for example scale-dependent primordial non-Gaussianity (Schmidt & Hui 2013; Byrnes & Tarrant 2015; Ashoorioon & Koivisto 2016; Adhikari et al. 2016; Byrnes et al. 2016; Adhikari et al. 2018; Hansen et al. 2019), direct-sum inflation (Kumar & Marto 2022; Gaztañaga & Kumar 2024), cosmic bounces (Agullo et al. 2021a,b), cosmic strings (Jazayeri et al. 2017; Yang et al. 2019) or loop quantum cosmology (Agullo et al. 2021b). However, before claiming any detection of primordial signature, it is necessary to fully characterize the different foregrounds that can leave an imprint in the CMB large-scale temperature fluctuations. At the level of the local Large Scale Structure (LSS), the presence of an unknown foreground has for example been claimed in Luparello et al. (2022) by cross correlating *Planck* and 2MRS data (see however Addison 2024, for a discussion about the significance of this detection). Around large spiral galaxies of the nearby Universe ($z < 0.02$), there is a significant decrease of the CMB temperature. Moreover, the overall corresponding signal reconstructed empirically seems to reproduce the low multipole behaviour of the CMB map (Hansen et al. 2023) and could even account for the cold spot (Lambas et al. 2024). More generally, the local LSS has been shown to contain its own features deviating from the cosmic mean, with a pancake shape structure of radius ~ 100 Mpc (Böhringer et al. 2021), an asymmetry between the northern and southern galactic hemispheres in stellar mass density (Karachentsev & Telikova 2018), and an under-density up to 200 Mpc (Whitbourn

* E-mail: gabriel.jung@universite-paris-saclay.fr

& Shanks 2014), except in our very close neighbourhood (~ 20 Mpc) because of the Virgo cluster.

Understanding to which extent these different anisotropic features of the local Universe can impact the CMB fluctuations is very challenging. A powerful tool to approach this issue is through constrained cosmological simulations, which can reconstruct accurately the local LSS and its physical properties. An extensive body of literature is devoted to generating such constrained simulations, utilising advanced N-body and hydrodynamical descriptions (see Vogelsberger et al. 2020, for a review) and initial conditions reconstructed from galaxy observations (see e.g., Bertschinger & Dekel 1989; Kravtsov et al. 2002; Kitaura & Enßlin 2008; Lavaux 2010; Jasche & Wandelt 2013; Wang et al. 2013; Heß et al. 2013; Sorce et al. 2014, 2016; McAlpine et al. 2022). The objective is to obtain a complete description of the distribution of matter and its properties, consistent with the known local LSS. The recent constrained hydrodynamical simulation called SLOW, generated from the initial conditions of Sorce (2018) with its large volume ($500 h^{-1}$ Mpc) and realistic baryonic physics as described in Dolag et al. (2023), enables detailed analyses of its different components, like the synchrotron emission (Böss et al. 2023) and the galaxy cluster properties (Hernández-Martínez et al. 2024).

In this work, we focus on the CMB secondary anisotropies related to the Sunyaev-Zeldovich (SZ) effect (Zeldovich & Sunyaev 1969; Sunyaev & Zeldovich 1972, 1980a,b) from the local Universe. We produce high-resolution full sky maps of its two components—thermal and kinetic—derived from the hot baryonic gas distribution in the SLOW simulation. We characterize these maps, firstly by measuring their power spectrum, which we compare to standard halo model predictions and to the outputs from previous hydrodynamical simulations, namely *Magneticum* (Dolag et al. 2016) and *Coruscant* Dolag et al. (2005). An extra care is taken to evaluate the role of the nearby Virgo cluster. On large angular scales, both the kSZ and tSZ signals are significantly dominated by the structures from the very local Universe, meaning they can carry some anisotropic large-scale features of the local LSS. We investigate their correlation with several well-known CMB large-scale anomalies, namely the lack-of-correlation, quadrupole-octopole alignment and hemispherical asymmetry. Moreover, we apply the analysis pipeline developed to study these anomalies to the latest *Planck* data release (PR4) (Planck Collaboration 2020b), confirming their presence at the reported levels from previous releases. This work is complementary to the analyses of (Gimeno-Amo et al. 2023) and (Billi et al. 2023), based on the same dataset.

This paper is organized as follows. In Sect. 2, we describe our simulated maps of the thermal and kinetic SZ effects from the local Universe. In Sect. 3, we recall different estimators of several CMB large-scale anomalies, and apply them to the latest *Planck* data (PR4). In Sect. 4, we characterize the statistical properties of the local tSZ and kSZ maps by studying their power spectra in a first time, and we examine to which extent they can contribute to the CMB large-scale anomalies. Finally, we draw our conclusions in Sect. 5.

2. Data and simulations

2.1. Hydrodynamical simulations

To construct the tSZ and kSZ signals from the local Universe, we use several hydrodynamical simulations which we present in this section. Our baseline simulation is SLOW, a recent and large constrained hydrodynamical simulation. We compare it to two

Ω_Λ	Ω_m	Ω_b	σ_8	n_s	h
0.692885	0.307115	0.0480217	0.829	0.961	0.6777

Table 1. Cosmological parameters of the SLOW constrained simulation, compatible with *Planck* observations (Planck Collaboration 2014a).

other simulations which have been studied in detail in the literature: the smaller constrained simulation *Coruscant*, and the unconstrained *Magneticum*, both to verify the impact of improvements in reconstructing the local large-scale structure, and how it differs from an average patch of our Λ CDM Universe.

2.1.1. The SLOW constrained simulation

SLOW is a hydrodynamical simulation reproducing the local Universe large-scale structure in a box of $500 h^{-1}$ Mpc. It contains 2×1536^3 dark matter and gas particles and assumes a *Planck*-like cosmology (see Table 1). For a detailed description of its production, we refer the reader to Dolag et al. (2023); Hernández-Martínez et al. (2024) and references therein, while here we summarise the most important steps.

The key ingredient of constrained simulations is the initial conditions, which are reconstructed from observations of the local Universe using different methods. For SLOW, initial conditions are derived from the CosmicFlows-2 data (Tully et al. 2013) following the approach described in Sorce (2018), based on the use of galaxy peculiar velocities to trace the full matter distribution.

Then, these initial conditions are evolved using the code OPENGADGET3 (Groth et al. 2023), developed from the standard TreePM code GADGET3 (Springel 2005) with an improved SPH solver (Beck et al. 2016). In addition to the standard gravitational evolution, the physics of baryonic matter (e.g., cooling, star formation, winds, AGN feedback) is included through advanced sub-grid models previously validated with the *Magneticum* hydrodynamical simulation (see Sect. 2.1.3).

2.1.2. The *Coruscant* constrained simulation

We consider another constrained simulation, called *Coruscant*, which focuses on the very local Universe. It describes indeed the local structures in a sphere of radius ~ 110 Mpc, embedded in a box of size $\sim 240 h^{-1}$ Mpc containing around 108 million particles in total (gas and dark matter). Initial conditions have been reconstructed from the observed galaxy density field in the IRAS 1.2-Jy survey (Fisher et al. 1995).

A first version of the simulation is described in detail in Dolag et al. (2005) (see also Mathis et al. 2002, for an earlier work based on similar initial conditions in the dark matter only case), and was later updated to include an earlier version of all the ingredients also used the *Magneticum* simulation. For other works analyzing this most recent version of the *Coruscant* simulation, see for example Planck Collaboration (2016b); Dolag et al. (2016); Coulton et al. (2022).

2.1.3. The *Magneticum* simulation

The last hydrodynamical simulation we study in this work is the *Box2* of the *Magneticum* simulation¹. Its unconstrained initial conditions are constituted of 2×1584^3 dark matter and gas particles in a box of size $352 h^{-1}$ Mpc, and the run includes the ingredients of baryonic physics detailed in Hirschmann et al. (2014); Dolag et al. (2016).

2.2. tSZ and kSZ maps of the local Universe

The large-scale structure of the Universe leaves imprints in the CMB anisotropies through different effects (for a review, see e.g., Aghanim et al. 2008). One of the most important is the thermal SZ effect (Zeldovich & Sunyaev 1969; Sunyaev & Zeldovich 1972). It consists of the inverse Compton scattering of CMB photons by electrons in the ionised gas mainly located in galaxy clusters, and is noted tSZ. The tSZ effect is proportional to the integral of the electron gas pressure along the line-of-sight. This corresponds to a spectral distortion of the CMB temperature fluctuations which can be written as

$$\frac{\Delta T^{\text{tSZ}}}{T_{\text{CMB}}}(\nu, \mathbf{\Omega}) = g(\nu)y(\mathbf{\Omega}), \quad (1)$$

where $g(\nu)$ is an overall factor depending on the frequency ν , and the Compton- y parameter describes the signal over the sky. These terms are given by

$$g(\nu) \equiv x \coth(x/2) - 4 \quad \text{with } x \equiv \frac{h\nu}{k_B T_{\text{CMB}}},$$

$$y(\mathbf{\Omega}) \equiv \frac{\sigma_T}{m_e c^2} \int_0^{r_{\text{CMB}}} dr P_e(\mathbf{\Omega}, r), \quad (2)$$

where h is the Planck constant, k_B is the Boltzmann constant, T_{CMB} is the CMB temperature, c is the speed of light and σ_T the scattering cross section. The electron gas pressure is $P_e = k_B n_e T_e$ with T_e , n_e and m_e the electron temperature, density and mass, respectively.

The kinetic SZ (kSZ) effect (Sunyaev & Zeldovich 1980a,b) is induced by the bulk motion of the electron gas moving with a peculiar velocity \mathbf{v}_e in the direction of the line-of-sight, and can be written as:

$$\frac{\Delta T^{\text{kSZ}}}{T_{\text{CMB}}}(\mathbf{\Omega}) = -\frac{\sigma_T}{c} \int_0^{r_{\text{CMB}}} dr \mathbf{\Omega} \cdot \mathbf{v}_e(\mathbf{\Omega}, r). \quad (3)$$

The kSZ effect has the same blackbody dependence as the CMB primary fluctuations. In amplitude, it is dominated by its tSZ counterpart, except when the tSZ effect is null at a frequency of about 220 GHz.

Using the numerical code SMAC² (Dolag et al. 2005), the integrands in Eqs. (2), (3) can be evaluated directly throughout the SLOW constrained hydrodynamical simulation for a HEALPix tessellation scheme, allowing to perform the integral in a range limited by the simulation volume. Pushing the integration further, for example to compute the full SZ signal, is also possible and requires to generate light-cones from the simulation (see Dolag et al. 2016, for an example based on the *Magneticum* simulation). However, here we are only interested in the SZ signal from the local Universe, and we restrict the computations to the volume of the SLOW simulation.

To obtain maps of the local tSZ (Compton- y) and kSZ signals, the integration starts from the observer position chosen so that the position of the largest simulated structures on the sky mimics as much as possible that of their observed counterparts.³ By construction of the constrained initial conditions, the observer position is very close to the center of the SLOW box. Then, to take advantage of the full constrained volume, we perform the integration up to 350 Mpc around it (the obtained maps will be referred to as SLOW-350). We also generate maps focused on the closest structures, up to 110 Mpc (constrained volume of *Coruscant*), from SLOW (the obtained maps will be referred to as SLOW-110) and *Coruscant*, both for comparison between the two generations of constrained simulations and for the direct study of close-by structures while avoiding contamination from the background. These maps, which have a resolution of $N_{\text{side}} = 1024$ (pixels of size ~ 3.4 arcmin) and constitute the core ingredient of this paper, are shown in Fig. 1.

On the largest scales, these maps are highly anisotropic as the signal is dominated by a few extended structures from the very local Universe. The most prominent one, localized on the upper right of each plot, corresponds to the Virgo galaxy cluster, and leads to a large positive/negative contribution in the tSZ/kSZ maps, respectively. Several other well-known galaxy clusters can be cross-identified in this simulation, with a good matching of position and mass, as discussed in detail in Hernández-Martínez et al. (2024).

There are however small differences between the observed and simulated positions in the sky of these clusters, as well as for their distance from the observer. These are mainly due to intrinsic limitations of the initial conditions reconstruction method making structures slightly displaced with respect to their expected position. To estimate the impact of these differences, we produce a set of maps (SLOW-near) where the observer position has been shifted 1 Mpc in different directions (14 new positions per maps) in the SLOW box. Note that we also tested a larger displacement of 2 Mpc, giving very similar conclusions.

Finally, to verify how the local tSZ and kSZ signals compare to random patches of the Universe, we generate sets of maps where the observer positions are selected in very distant positions (more than 100 Mpc between each) in both SLOW (SLOW-grid) and *Magneticum* (27 maps for each). This allows us to obtain almost independent realizations of the SZ signals.

A list of the different maps used in this work and of their main characteristics is given in Table 2. Their statistical properties are discussed in details in Sect. 4.

2.3. Planck CMB data

For the analyses presented in Sect. 3, we use the CMB temperature datasets from the latest *Planck* release, (for details about the PR4 release, see Planck Collaboration 2020b). This includes foreground-cleaned CMB maps produced by the component separation methods SEVEM (Fernandez-Cobos et al. 2012) and Commander (Eriksen et al. 2008), available on the *Planck* Legacy Archive⁴ (PLA). We also use the associated simulated CMB maps (600 and 100 for SEVEM and Commander, respectively), accessible from NERSC⁵ (National Energy Research Scientific Computing Center).

³ To be exact, we start the integration at 5 Mpc from the observer, removing the Milky Way foreground effect as well as all galaxies in the local Group.

⁴ <http://pla.esac.esa.int/pla/>

⁵ <https://portal.nersc.gov/project/cmb/planck2020/>

¹ <http://www.magneticum.org/simulations.html>

² <https://www.mpa-garching.mpg.de/~kdolag/Smac/>

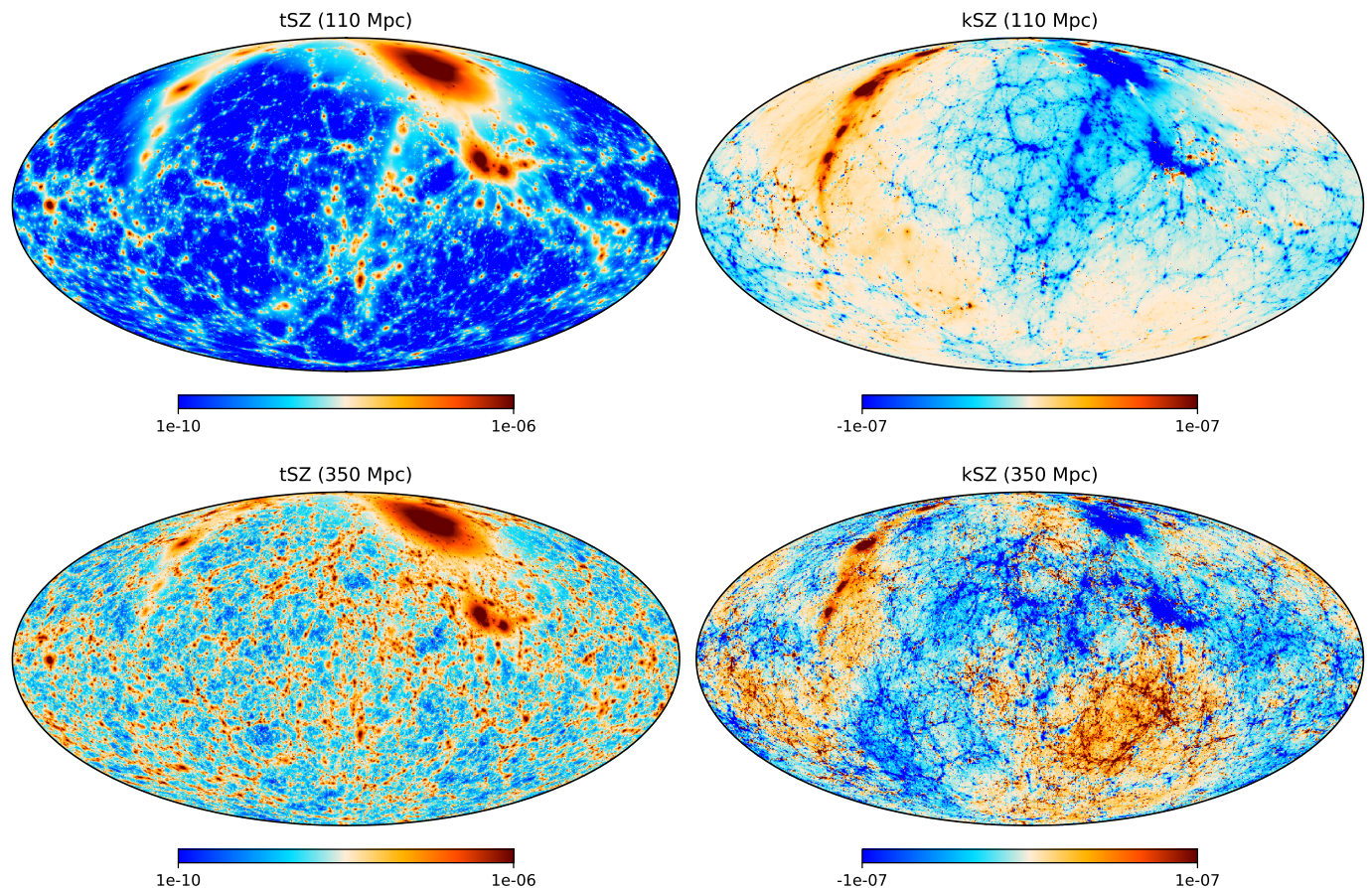


Fig. 1. tSZ (y-Compton) and kSZ signals from the local Universe in the SLOW constrained simulation. The upper panels only include the most local structures (up to 110 Mpc, denoted as SLOW-110) while the lower ones use almost the full volume of the box (up to 350 Mpc, denoted as SLOW-350). Note that the colour scale is logarithmic in the tSZ maps and symmetric logarithmic for the kSZ maps. The main characteristics of these maps are recalled in Table 2.

Name	Description	Number	r_{\max} (Mpc)	N_{side}
SLOW-110	Local Universe (from SLOW)	1	110	1024
SLOW-350	Local Universe (from SLOW)	1	350	1024
SLOW-near	Near local Universe (observer position moved by 1 Mpc)	14	110	1024
SLOW-grid	Grid of observer positions all over the SLOW simulation	27	110	1024
MAGNETICUM	Same as SLOW-grid , for the <i>Magneticum</i> simulation	27	110	1024
CORUSCANT	Local Universe (from <i>Coruscant</i>)	1	110	1024

Table 2. tSZ and kSZ maps constructed from the SLOW, *Magneticum* and *Coruscant* hydrodynamical simulations used in this work, and their main characteristics.

The main mask used in this work is the 2018 *Planck* common mask. In addition, to check the robustness of our results against astrophysical contamination, we also consider masks covering a larger area near the galactic plane. All these masks are found in the PLA.

Since we are primarily interested in large-scale effects, we do not work directly with the data at full resolution ($N_{\text{side}} = 2048$, and a Gaussian beam with a FWHM of $5'$), and use instead a downgraded resolution ($N_{\text{side}} = 64$, and $160'$ Gaussian beam), as in Planck Collaboration (2020a). For the masks, after downgrad-

ing, we set all pixels with a value below 0.95 to 0 to keep them binary.

Before estimating the different statistics of interest introduced in the following section, the masks are applied to the CMB *Planck* data maps and their simulated counterparts. We then remove the monopole and dipole of the resulting masked maps. As the mask itself can have a strong impact on the large-scale statistics we will measure, it is necessary to fill in the masked regions. Here, we use the diffusive inpainting technique (see for example Gruetjen et al. 2017, for details).

3. Large-scale anomalies in *Planck* CMB data

In this section, we investigate several well-studied large-scale anomalies of the CMB temperature anisotropies, using the most recent data available from *Planck* (PR4, see Sect. 2.3 for details). For each anomaly, we recall briefly its historical definition and a corresponding standard estimator, before applying it to the *Planck* observed and simulated CMB maps.

3.1. Lack of correlation

One surprising feature of the CMB anisotropies, first observed in *COBE* data (Hinshaw et al. 1996), is that the two-point angular correlation function $C(\theta)$ (2PACF) seems to vanish on large angular scales ($\theta > 60^\circ$).

To quantify this so-called lack of correlation, the standard choice of statistic is the quantity noted $S_{1/2}$ and written as,

$$S_{1/2} \equiv \int_{-1}^{1/2} [C(\theta)]^2 d(\cos \theta). \quad (4)$$

It was originally introduced in (Spergel et al. 2003), and used in many works based on *WMAP* or *Planck* data (see for example Copi et al. 2007, 2009; Gruppuso 2014; Copi et al. 2015a; Schwarz et al. 2016; Planck Collaboration 2014b, 2016a; Muir et al. 2018; Planck Collaboration 2020a; Jones et al. 2023). We follow the computation steps of Copi et al. (2009), where $S_{1/2}$ is evaluated directly from (pseudo) power spectrum measurements.

To estimate these pseudo- C_ℓ from the *Planck* CMB maps, we use the numerical code NaMaster⁶ described in Alonso et al. (2019) (for earlier works on pseudo- C_ℓ estimation, see Wandelt et al. 1998; Hivon et al. 2002; Hansen et al. 2002; Tristram et al. 2005). Note that with this method, constructed to handle masked maps, we do not need to perform the inpainting step after applying the *Planck* common mask.

Our results are shown in Fig. 2. As known since *COBE* observations (Bennett et al. 1993), which were later confirmed in *WMAP* data (Spergel et al. 2003), the observed quadrupole has a low amplitude, among the lowest of the simulations (2.5% and 5% of the lowest in SEVEM and Commander simulations, respectively). The octopole moment is also rather low (15th percentile). Note however that this cannot be considered as anomalous, as was shown in (Efstathiou 2003), and does not explain the lack of correlation effect by itself.

In Fig. 3, we show the quantity $S_{1/2}$ computed from the *Planck* PR4 pseudo- C_ℓ of Fig. 2. It can directly be seen that the observed value is lower than in all the simulations, confirming that the 2PACF is anomalously close to zero on angular scales ($\theta > 60^\circ$).

3.2. Alignment of the quadrupole and octopole

Another striking feature of the CMB temperature fluctuations is the alignment of the quadrupole and octopole (first reported in *WMAP* data de Oliveira-Costa et al. 2004), which can be studied using multipole vectors (Maxwell 1865; Copi et al. 2004; Dennis 2004). These multipole vectors constitute an alternative to the standard decomposition of CMB anisotropies into spherical harmonics, where the information contained in each multipole ℓ is given by a real constant and ℓ unit vectors \mathbf{v}_ℓ^j (with $j = 1 \dots \ell$).

To estimate low- ℓ multipole vectors in the *Planck* PR4 maps, we use the optimised numerical code polyMV⁷ presented in

⁶ <https://github.com/LSSTDESC/NaMaster>

⁷ <https://oliveirara.github.io/polyMV/>

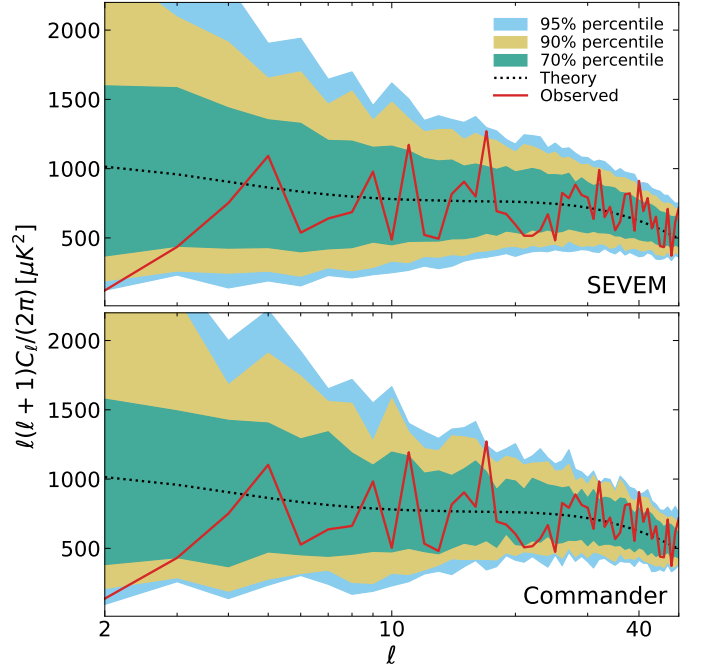


Fig. 2. Pseudo- C_ℓ of the *Planck* PR4 CMB temperature maps, from SEVEM (top panel) and Commander (bottom panel). The red solid lines are measured from cleaned observed maps and the black dotted lines are theoretical predictions computing using CAMB. The colored areas are determined from simulations, and show their distribution around the median. For both component separation methods, the observed quadrupole is among the 5% lowest simulated values (only 15 SEVEM simulations out of 600 have a lower quadrupole, and 4 for Commander). Only 15% of the simulations have a smaller octopole.

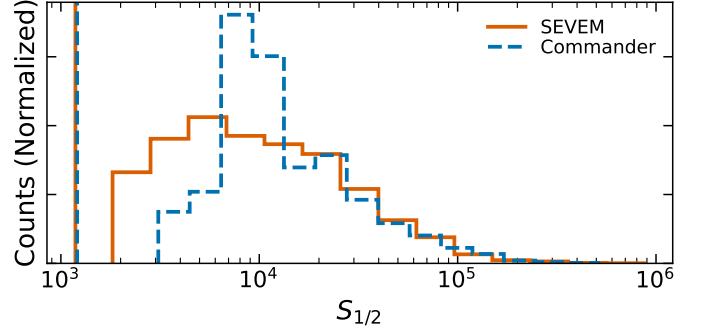


Fig. 3. Lack of correlation on large angular scales ($\theta > 60^\circ$) in the cleaned *Planck* PR4 CMB temperature maps. We show the distribution of the statistic $S_{1/2}$ (Eq. 4) measured in the *Planck* PR4 simulations, and the vertical lines (on the left) are the observed values. Blue dashed lines and orange solid lines correspond to Commander and SEVEM maps, respectively. None of the measured $S_{1/2}$ in simulations is as low as in observations.

Oliveira et al. (2020). We then follow the analyses of Schwarz et al. (2004); Copi et al. (2006) where the key ingredient to study alignments is the "area vectors" defined as cross-products between multipole vectors at a given ℓ ,

$$\mathbf{w}_\ell^{(i,j)} \equiv \mathbf{v}_\ell^i \times \mathbf{v}_\ell^j. \quad (5)$$

There is thus one vector \mathbf{w}_2 for the quadrupole, corresponding to one preferred direction, and three ($\mathbf{w}_3^1, \mathbf{w}_3^2, \mathbf{w}_3^3$) for the octopole. To measure the alignment of the octopole with any given direc-

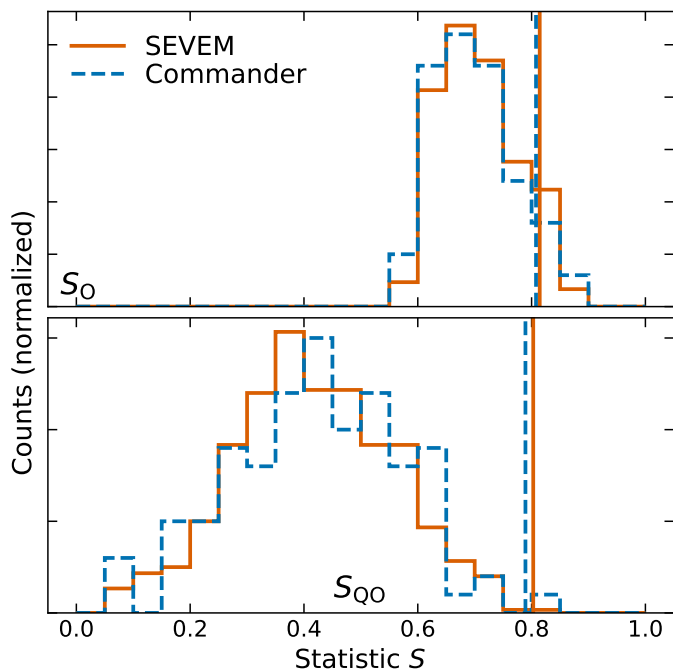


Fig. 4. Quadrupole-octopole alignment in the cleaned *Planck* PR4 CMB temperature maps. In the upper panel, we show the distribution of S_O (see eq. 6), indicating how planar the octopole is. Larger values are obtained for 59 SEVEM simulations (out of 600) and 9 (out of 100) for Commander. In the lower panel, we show the distribution of S_{QO} , measuring the alignment between quadrupole and octopole. Only one simulation, in both sets, has a larger S_{QO} value than the observed data. Solid orange and dashed blue lines correspond to SEVEM and Commander maps, respectively.

tion in the sky Ω , one can compute the following quantity

$$S(\Omega) \equiv \frac{1}{3} \sum_{i=1}^3 \Omega \cdot w_3^i. \quad (6)$$

We are interested in two specific values of $S(\Omega)$: its maximum and $S(w_2)$. We will denote them as S_O and S_{QO} in the following. The first measures how aligned are the three area vectors of the octopole and defines its averaged preferred direction, while the second estimates the alignment between the quadrupole and octopole.

In Fig. 4, we show the distribution of S_O and S_{QO} determined from the *Planck* PR4 simulated maps and their observed counterparts. Only 10% of the simulations have a larger value of S_O , confirming that its three area vectors are relatively aligned, the so-called planarity of the octopole. By itself, this does not constitute an anomaly, but this allows the high value of S_{QO} , very close to S_O . Such an alignment of the quadrupole and octopole is only found in one of the simulated CMB maps of each set.

In Fig. 5, we show the quadrupole and octopole preferred directions determined from the *Planck* PR4 CMB maps, after applying the common mask and inpainting the masked areas, as described in Sect. 2.3. As expected from the measured values of S_{QO} , the two favored axes point in the same area of the sky. The corresponding direction is close to the ecliptic plane and points toward the position of the Virgo cluster.

3.3. Hemispherical Asymmetry

An efficient method to study large-scale anisotropies of the CMB is the use of position-dependent statistics. It consists in divid-

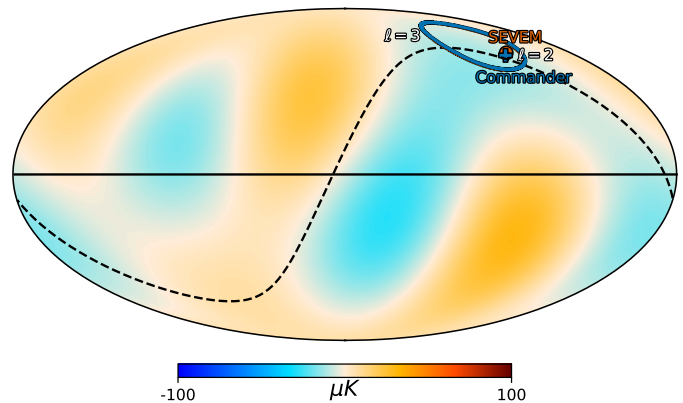


Fig. 5. Quadrupole-octopole alignment in the cleaned *Planck* PR4 CMB temperature maps. The preferred direction of the quadrupole is given by the orange circle and blue crosses for SEVEM and Commander, respectively. The orange and blue contours, which are almost superimposed, correspond to the areas where $S(\Omega)$ (defined in Eq. 6) is within 3% of its maximum (preferred direction of the octopole), for SEVEM and Commander respectively. The background map is the sum of the SEVEM CMB quadrupole and octopole. The black solid and dashed lines correspond to the galactic and ecliptic planes, respectively. Note that we only show the preferred directions in the northern galactic hemisphere.

ing the sky into a set of equal-sized and uniformly distributed patches, and then computing, patch-by-patch, a chosen statistic to measure its variation over the celestial sphere. Depending on the considered statistics, as well as the patch properties (e.g., size, shape), different physical effects and scales can be probed.

For example, simply measuring the pixel variance in each patch is a very powerful probe of the hemispherical asymmetry (known since *WMAP*, see e.g. Eriksen et al. 2004). This position-dependent variance (or local-variance) estimator was originally introduced in Akrami et al. (2014), and applied to the different releases of *Planck* data (for a recent analysis of the PR4 data, see Gimeno-Amo et al. 2023). Here, we extend the analysis to higher-order moments, namely the skewness and kurtosis, and in appendix A we also compute the position-dependent power spectrum.

Our patches are constructed from a very low resolution HEALPix map ($N_{\text{side}} = 8$), setting one pixel to one and the rest to zero, and upgrading its resolution to the same as the maps we analyze (here $N_{\text{side}} = 64$). Repeating the process for each pixel of the low resolution maps gives a set of 768 patches covering the full sky, without any overlapping areas. In appendix B, we repeat our analysis considering discs of 4° radius, the main patch choice of Planck Collaboration (2020a); Gimeno-Amo et al. (2023). Both sets lead to the similar conclusions, with a higher statistical significance for the discs which have been fine-tuned for the study of the hemispherical asymmetry.

We measure the temperature variance in patches of the *Planck* PR4 CMB maps at low resolution (and the simulated CMB maps), after applying the common mask. Patches with more than 90% of masked pixels are excluded, following the analysis of Planck Collaboration (2020a). For each patch of every map, we then subtract the average value and divide by the variance computed from the corresponding set of simulations. The resulting maps are called position-dependent variances in the rest of the section. Position-dependent skewness and kurtosis maps are obtained following the same method.

	Variance	Skewness	Kurtosis
SEVEM	2.3	50.8	61.3
Commander	1	55	17

Table 3. Percentages of *Planck* PR4 simulations with a larger dipole amplitude A_d of the position-dependent variance, skewness and kurtosis than in observations, computed from 600 simulations for SEVEM, and 100 for Commander, and using HEALPix pixel patches. Only 1 Commander simulation and 14 SEVEM simulations have a larger dipole amplitude for the variance.

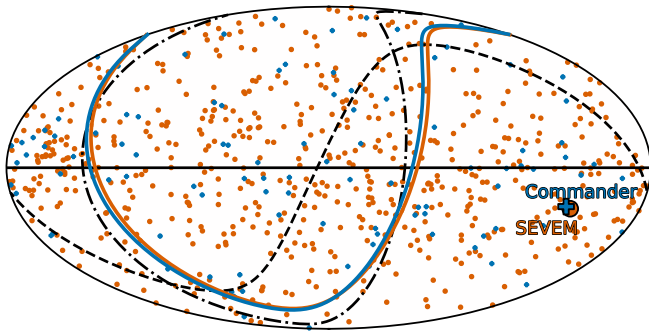


Fig. 6. Preferred direction of the variance asymmetry in the *Planck* PR4 CMB temperature maps. Dipoles are computed from the position-dependent variance maps computed using HEALPix pixel patches. The data dipole directions are given by the large blue crosses and orange discs for Commander and SEVEM, respectively, and the small markers are for the corresponding simulations. The blue and orange lines are the planes orthogonal to these observed dipoles. The solid, dashed and dashdotted lines correspond to the galactic, ecliptic and supergalactic planes, respectively.

To verify the presence of any hemispherical asymmetry, one can fit a dipole to these position-dependent variances (and higher-order moments). Its amplitude A_d can confirm, or not, the presence of an asymmetry in the maps, and its direction is orthogonal to the plane defining the two hemispheres. In Table 3, we compare the data dipole amplitude to the simulations, and verify the well-known result that in the variance case it is larger than for the vast majority of the simulated CMB maps, at the 1-2% level. No dipolar asymmetry is observed for the skewness and kurtosis. Then in Fig. 6, we show the corresponding directions on the sky of the position-dependent variance dipoles. The dipole directions of the different simulated CMB maps point all over the sky, confirming that there is no preferred axis inherent to our analysis pipeline (e.g., masking choices). The observed axis of asymmetry is relatively close to the supergalactic plane, where many large-scale structures of the local Universe can be observed (e.g., the Virgo, Coma, Centaurus or Perseus clusters). In Sect. 4.2, we will apply the same method to the local Universe simulations to check if its tSZ and kSZ contributions can explain the observed asymmetry.

Finally, we use the plane orthogonal to the measured dipole of each position-dependent statistic map in order to separate the map into two hemispheres, and we average it over these two halves of the sky. Results are shown in Fig. 7, where we compare the distribution of the different averaged quantities over the full sky, and the hemispheres in the dipole direction and opposite to it. In the direction opposite to the dipole in the observed data (close to the supergalactic northern hemisphere) the

position-dependent variance is very low (among the 3% lowest CMB simulated maps for the discs as verified in appendix B), while the other hemisphere does not show any deviation. Note that splitting the sky in two halves on either sides of the ecliptic plane gives similar results, with a very low variance in one of the hemispheres. For the skewness, no such effect is seen, and this is also the case when splitting the sky using the ecliptic or supergalactic planes. In the *Planck* map obtained from Commander we observe a large position-dependent kurtosis, even in the full sky case, and with a non-negligible difference with the SEVEM results. We have verified that the excess is localized in the supergalactic and ecliptic south hemispheres, but no specific source can be easily identified. While there is a difference between the two hemispheres, no strong dipolar modulation was detected for the kurtosis as reported in Table 3, and thus we cannot directly relate this issue with the hemispherical asymmetry anomaly.

4. Characterizing the tSZ and kSZ effects from the local Universe

In this section, we explore further the statistical large-scale properties of the tSZ and kSZ effects from constrained simulations of the local Universe. In a first part, we focus on the power spectrum, while in a second part, we evaluate the impact of the secondary anisotropies induced by the local Universe on the different large-scale CMB anomalies studied in Sect. 3.

4.1. SZ power spectra from the local Universe

We measure power spectra from the different maps shown in Fig. 1 (see also Table 2). This includes tSZ and kSZ maps for both volumes of local Universe ($r_{\max} = 110, 350$ Mpc), as well as $r_{\max} = 110$ Mpc maps where the observer position is slightly or largely displaced in the SLOW simulation.

For comparison purposes, we compute theoretical predictions of the tSZ power spectrum using the emulator described in Douspis et al. (2022), trained on the halo model developed in Salvati et al. (2018), and of the kSZ power spectrum using the numerical code `class_sz`⁸ (Bolliet et al. 2023)⁹, considering three different redshift ranges of integration (two correspond to the local Universe volumes and the third to an integration up to $z = 4$).

In Fig. 8, we compare these theoretical predictions to the power spectra from the simulated maps. We focus on the large scales ($\ell \leq 150$), where the local tSZ and kSZ effect are expected to either dominate or to contribute significantly to the full SZ signal, as verified by theoretical calculations. This shows the agreement between these theoretical predictions and the range (defined as a 90% percentile) spanned by the SLOW-grid set, with a few exceptions that we now discuss.

For $\ell \leq 70$, the tSZ power spectrum from the local Universe is well above the SLOW-grid range, and up to one order of magnitude larger than the theoretical prediction. Small uncertainties on the Milky Way position in the simulation, obtained with the SLOW-near set, have a much smaller effect on this power spectrum, at most of order 20%. In addition, for $\ell < 30$ the tSZ signal is due almost entirely to the very local Universe ($r_{\max} = 110$ Mpc map). Similarly, the local Universe kSZ contribution is also at the high limit of the expected range, with, again, the very local Universe representing a large part of the signal.

⁸ https://github.com/CLASS-SZ/class_sz

⁹ `class_sz` is based on the `class` code <http://class-code.net/> (Blas et al. 2011)

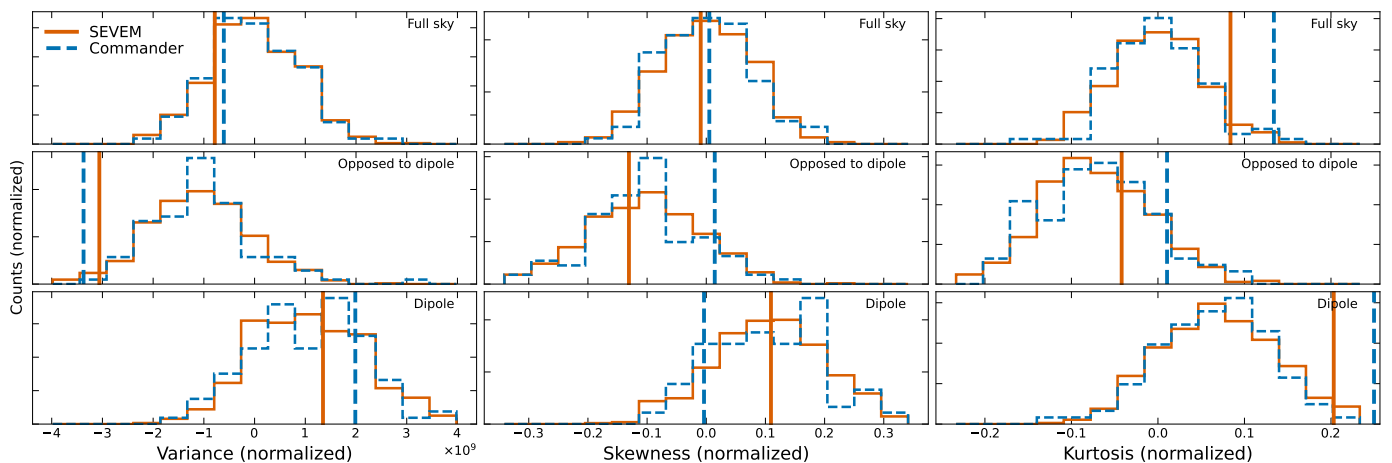


Fig. 7. Hemispherical asymmetry in the *Planck* PR4 CMB temperature data. From left to right, we show the position-dependent variance, skewness and kurtosis averaged over the full sky (upper row), and the two hemispheres defined by the plane orthogonal to the position-dependent variance of each individual map (opposed and same directions as the dipole in the middle and lower rows, respectively). The orange and blue vertical lines correspond to the observed SEVEM and Commander maps, respectively, and the histograms are obtained from the corresponding 600 SEVEM (orange), and 100 Commander (blue) simulations. There is a lack of variance in the hemisphere opposed to the dipole, where 583 (out of 600) SEVEM and 99 (out of 100) Commander simulations have larger values than the data.

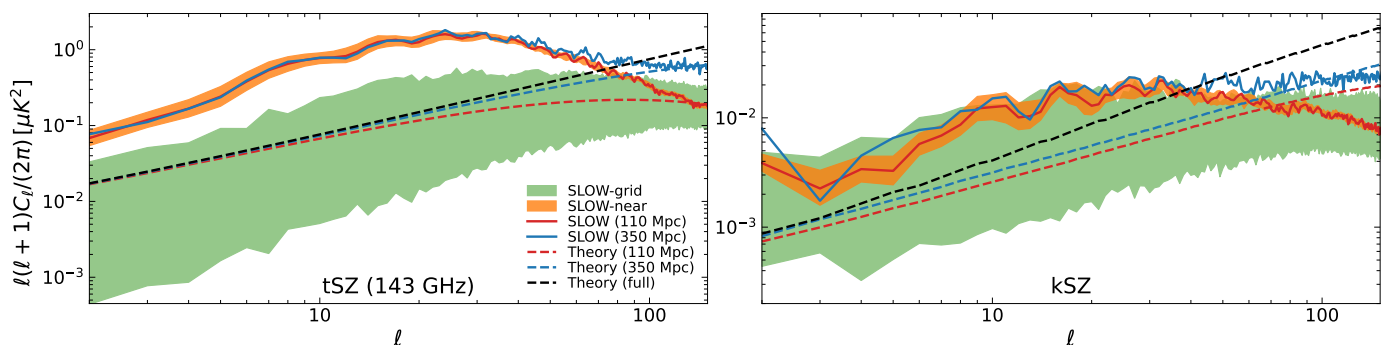


Fig. 8. Local tSZ (left) and kSZ (right) power spectra, compared to the average. The red and blue solid lines are power spectra measured from the maps shown in Fig. 1, constructed by integrating electron gas properties through the SLOW simulation from the Milky Way position to $r_{\max} = 110$ and $r_{\max} = 350$ Mpc, respectively. The colored areas are 90% percentiles determined from the sets of maps where the center for integration is displaced in the SLOW simulation, slightly (by 1 Mpc from the Milky Way) in orange (SLOW-near), and largely (more than 100 Mpc between each center) in green (SLOW-grid). The dashed lines are theoretical predictions computed in halo model, where the red and blue lines are integrated up to $r_{\max} = 110$ and $r_{\max} = 350$ Mpc, and the black lines correspond to the full tSZ/kSZ expected signals. The tSZ power spectrum is shown at the frequency 143 GHz.

As we now verify by applying different masks, the large amplitude of the local Universe tSZ power spectrum at low ℓ is related to the simulated replica of the Virgo cluster. We apply a 10° radius disc mask centered on the Virgo cluster to the local Universe tSZ and kSZ maps (tests with smaller discs show that there are not sufficient to remove the full contribution of Virgo). Similarly, we construct one mask for each map of the SLOW-grid and SLOW-near sets, removing the contribution of the most prominent cluster in each map. This most prominent cluster is identified with the following procedure consisting in downgrading the tSZ maps to a resolution of $N_{\text{side}} = 32$ and using the pixel with the largest value as the center of the disc mask. With this method, the Virgo cluster is always selected in the SLOW-near simulations, as intended.

Power spectra computed on these masked simulations of the tSZ and kSZ effects are shown in Fig. 9. Removing the contribution of the Virgo cluster decreases the tSZ power spectrum at low ℓ by more than an order of magnitude, bringing it in the range given by the SLOW-grid set, although still in the high part. Masking Virgo, the kSZ power spectrum is brought within the

average on large scales. Moreover, masking the most prominent cluster has a smaller effect on most of the simulations than in the local Universe case, decreasing the tSZ signal by a factor 2 on average. In the SLOW-grid set of 27 simulations, only one simulation has a similar decrease after masking, confirming the relatively low chance of having a large contribution from a cluster sufficiently close and large as Virgo.

We also mask individually several other identified clusters of the local Universe identified in Hernández-Martínez et al. (2024). The only one contributing significantly to the power spectrum is Centaurus, dominating the signal around $\ell \sim 50$. In Fig. 10, we verify that masking both Virgo and Centaurus indeed removes most of the SLOW-110 tSZ and kSZ signals, and the difference with the SLOW-350 power spectra finally becomes significant. In addition, the local Universe is now in the lower end of the SLOW-grid range. This is consistent with the main conclusions of Sorce et al. (2016); Dolag et al. (2023), where it is reported that the simulated local Universe is under-dense up to 200 Mpc, in agreement with observations (see e.g. Whitbourn & Shanks 2014). Note however that the simulated equivalent of

the Centaurus cluster of SLOW has been shown in Hernández-Martínez et al. (2024) to be close to five times more massive than expected, making its simulated SZ contribution also larger.

For further comparisons, we measure power spectra from the maps derived from the constrained *Coruscant* and unconstrained *Magneticum* hydrodynamical simulations, presented in Sects. 2.1.2 and 2.1.3, respectively. The corresponding results are shown in Figs. 11 (full sky) and 12 (with the most prominent cluster masked, e.g., Virgo in the case of the local Universe). Due to the different characteristics of each simulation (cosmological parameters, resolution, box sizes) a perfect agreement is not expected. To take into account the dependence on cosmological parameters, we rescale the tSZ power spectra of the *Coruscant* and *Magneticum* maps using $C_\ell^{\text{tSZ}} \propto \sigma_8^3 \Omega_m^3$ (Hill & Pajer 2013). Similarly, the *Coruscant* and *Magneticum* kSZ power spectra are rescaled using the factor between the theoretical predictions obtained for the different cosmologies.

One important difference between the two generations of constrained simulations (SLOW and *Coruscant*) is the impact of the Virgo cluster on large scales. In *Coruscant*, no excess of signal is observed on these scales, making it one order of magnitude below SLOW. However, after masking Virgo, the tSZ and kSZ power spectra of both maps match extremely well up to $\ell \sim 20$ (tSZ) and $\ell \sim 100$ (kSZ), before other effects like the resolution of the box play a role. For the kSZ power spectrum, we can also see that removing the Virgo contribution has a much stronger effect in SLOW.

We can can also see that the SLOW-grid set of maps spans a larger range of values than its equivalent set from *Magneticum* on large scales ($\ell \leq 30$), which indicates that in the *Magneticum* set it is even more unlikely to have a cluster like Virgo (close and large enough to totally dominate the signal). One possible explanation is the fact that, as reported in Sorce et al. (2016); Dolag et al. (2023), the local Universe contains a significant overdensity of very massive clusters (masses above $10^{15} M_\odot$) in a large volume around our position (up to $r_{\text{max}} = 200$ Mpc) with respect to the *Magneticum* simulation (although not exactly the same as here). This could make more likely to have a massive cluster in the neighbourhood of the different centers used in the SLOW-grid set.

In conclusion, this highlights two interesting properties of the local tSZ and kSZ power spectra on large scales, compared to other volumes of the same size selected randomly. The local power spectra are dominated by a very low number of clusters, mainly Virgo and Centaurus. Despite this, the low- ℓ tSZ power spectrum is larger than in the majority of the other simulated maps (around 95%), mainly due to the fact that the Virgo cluster is so close from us. Its signal expands on a large area of the sky, as a disc of 10° radius is necessary to mask it fully, much wider than the 2° radius disc of the *Planck* common mask for example. Therefore, in the following section, we evaluate if this larger than expected local SZ signal can significantly modify the statistical properties of the CMB on very large angular scales.

4.2. Local tSZ and kSZ effects and CMB large-scale anomalies

We use the simulated maps of the tSZ and kSZ effects from the local Universe, shown in Fig. 1, to investigate the impact they have on the largest angular scales of the CMB. On these scales, several so-called anomalies (see Sect. 3) have been observed, with hints of correlation with the local Universe (e.g., alignments of low multipoles near the Virgo direction, axis of asymmetry close to the supergalactic plane).

For this purpose, we produce CMB realizations including the local tSZ and kSZ effects. We start by generating 10000 CMB Gaussian realizations from the *Planck* best-fit theoretical power spectrum computed with CAMB, with a resolution of $N_{\text{side}} = 64$ and a Gaussian beam with a FWHM of $160'$, which is the same as the *Planck* maps described in Sect. 2.3. To each of these Gaussian CMB simulations, we add the tSZ and kSZ signal from the local Universe obtained from the constrained simulations at a chosen frequency, after degrading the maps resolution to $N_{\text{side}} = 64$ and applying the $160'$ Gaussian beam (again, the same as the *Planck* maps). We mask the galactic plane, and in some cases Virgo (with a 10° radius disc) keeping almost 70% of the sky for the analysis. Finally, we compute the different estimators of CMB large-anomalies described in Sect. 3 in both the Gaussian CMB simulations and their CMB + SZ counterparts to compare the differences.

We report our main results in Figs. 13, 14 and 15, focusing on the lack of correlation, quadrupole-octopole alignment and hemispherical asymmetry anomalies, respectively. We use as our baseline the $r_{\text{max}} = 350$ Mpc maps, with a frequency of 143 GHz for the tSZ signal. Tests with the lower r_{max} , other frequencies, 100 and 217 GHz in particular, or in a full sky case, were performed and lead to similar results.

The main conclusion is the same for the three anomalies, the SZ effect from the local Universe affects the different quantities by a few % at most, far below the level of the anomalies. For example, the observed $S_{1/2}$ is less than half of the smallest value of all the simulated *Planck* CMB maps (itself being a few times smaller than the average). Similarly moving the observed S_{QO} by 2% would still leave it in the tail of the distribution of alignments in the simulated *Planck* CMB maps. Moreover, there is no visible preferred sign, meaning that on average its effect on the distribution of the different statistics is even much smaller.

When we focus on the simulations which are "anomalous" (i.e., the different estimators are in the tail of the expected distribution, at a level not so far from the *Planck* ones), the impact of the SZ effect from the local Universe is even smaller. The effect is at most slightly stronger when Virgo is not masked at all, meaning that, despite its domination of the SZ signal at low multipoles, its effect on CMB large-scale anomalies is only a very small contribution.

5. Conclusion

In this paper, we have explored the impact of the local Universe through the tSZ and kSZ effects on the CMB temperature anisotropies at large scales. Our objective were twofold, characterizing the large scale properties of the CMB temperature fluctuations with a new analysis of the large-scale anomalies of the latest *Planck* data, and verifying their correlation with the local tSZ and kSZ signals, obtained from advanced constrained hydrodynamical cosmological simulations.

Using the constrained hydrodynamical simulation SLOW, reproducing a large volume of the nearby LSS, we have constructed high-resolution maps of the local tSZ and kSZ effects. We have shown that they are the dominant contributions of the overall expected tSZ and kSZ effects on large angular scales, by comparison to theoretical predictions, and thus leaves anisotropic features correlated to the local Universe in the large-scale fluctuations of the CMB. We have characterized the local tSZ and kSZ signals mainly by looking at their power spectrum, highlighting their strong dependence to a few specific structures in the maps. First tests with higher order statistics like the bispectrum, which are beyond the scope of this work and will be

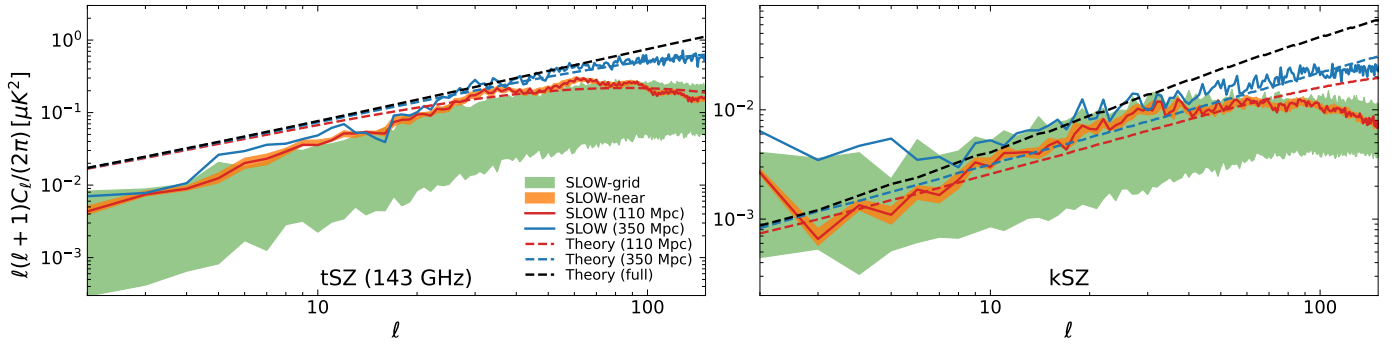


Fig. 9. Same as Fig. 8, where the most prominent cluster in each simulation has been masked by a 10° radius disc. In the local Universe, this corresponds to the Virgo cluster.

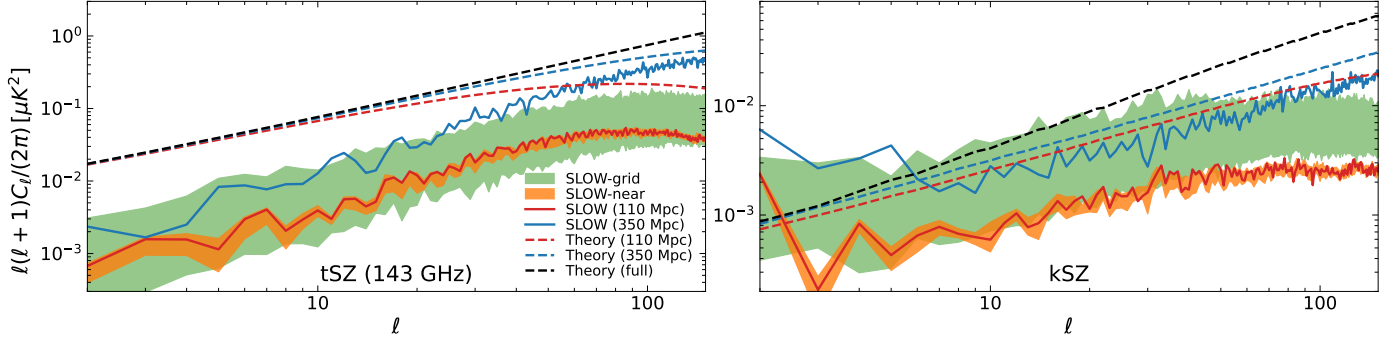


Fig. 10. Same as Fig. 8, where the two most prominent clusters in each simulation has been masked by a 10° radius disc. In the local Universe, this corresponds to the Virgo and Centaurus clusters.

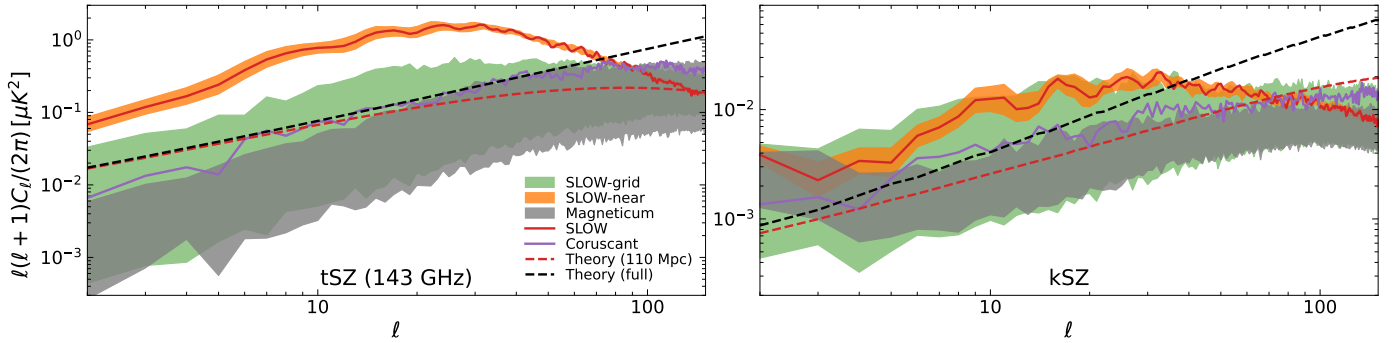


Fig. 11. tSZ and kSZ power spectra, up to $r_{\text{max}} = 110$ Mpc, from several hydrodynamical simulations. As in Fig. 8, the red solid line, orange and green areas are determined from the SLOW simulation, and the dashed lines are the corresponding halo model predictions. The purple solid lines are estimated from local Universe maps determined from the *Coruscant* simulation, and the grey areas are 90% percentiles from the *Magneticum* simulation.

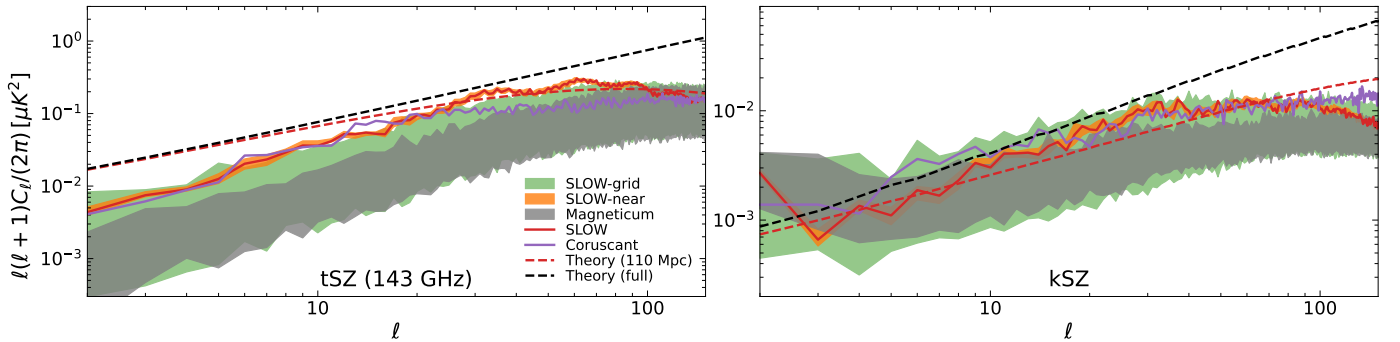


Fig. 12. Same as Fig 11, where the most prominent cluster have been masked in each map.

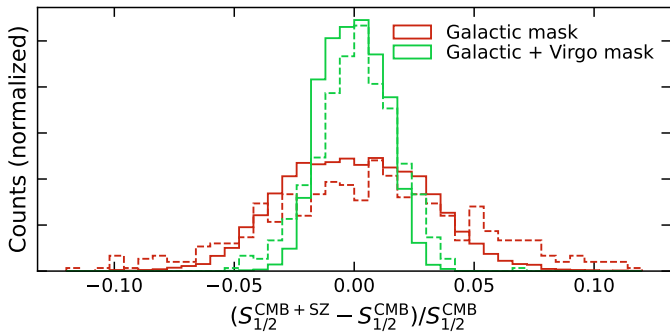


Fig. 13. Impact of the local Universe SZ signal on the lack of correlation at angular scales $\theta > 60^\circ$. We measure the difference of $S_{1/2}$ (see Eq. 4) between Gaussian CMB realizations including or not the local tSZ (at 143 GHz) and kSZ effects, when masking the galactic plane only (in red), and both the galactic plane and Virgo (in green). Distributions are shown for both the full set (solid lines) and the 5% (dashed) simulations where the lack of correlation is the strongest (smallest $S_{1/2}$).

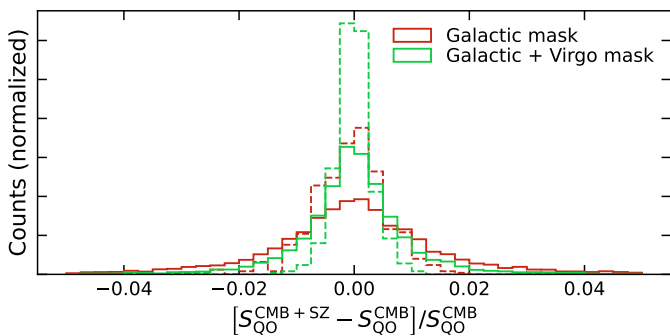


Fig. 14. Impact of the local Universe SZ signal on the quadrupole-octopole alignment. We measure the difference of S_{Q0} (see Eq. 6) between Gaussian CMB realizations including or not the local tSZ (at 143 GHz) and kSZ effects, when masking the galactic plane only (in red), and both the galactic plane and Virgo (in green). Distributions are shown for both the full set (solid lines) and the 5% (dashed) simulations where the alignment is the strongest (largest S_{Q0}).

discussed in future works, lead to similar conclusions. In particular, the Virgo cluster is responsible for most of the large-scale signal. Moreover, this signal is stronger than in $\sim 95\%$ of the other random patches of the universe that we tested, both by moving the observer position in the SLOW simulation or using the unconstrained *Magneticum* simulation. Both the localisation and higher than expected amplitude of the local Universe tSZ and kSZ signals led to the need for further investigation of their impact on the large-scale CMB temperature fluctuations, for example based on the methods developed for the study of the CMB large-scale anomalies.

We have analyzed several of the CMB temperature large-scale anomalies in the latest *Planck* temperature data (PR4)—the lack-of-correlation using the quantity $S_{1/2}$, the quadrupole-octopole alignment using multipole vectors and the hemispherical asymmetry with a local variance approach. Our analysis, conducted on cleaned CMB maps from both *Commander* and *SEVEM*, leads to similar conclusions as other analyses conducted on previous datasets (see e.g., Planck Collaboration 2020a, for PR3 results), or (Gimeno-Amo et al. 2023; Billi et al. 2023, on PR4). These unexpected deviations from isotropy are observed at a level found in typically less than 1% of the *Planck* CMB simulated maps, with some properties, such as a preferred direction of the quadrupole and octopole in the Virgo region and an

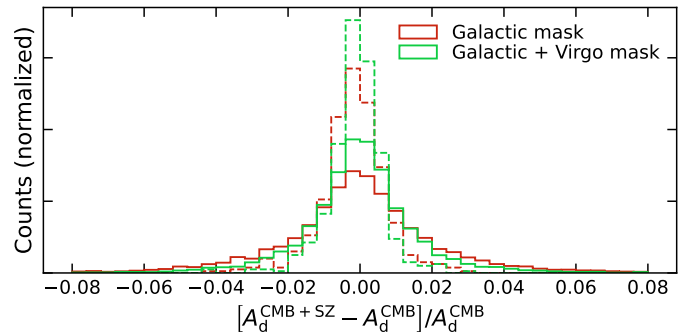


Fig. 15. Impact of the local Universe SZ signal on the hemispherical asymmetry. We measure the difference of A_d (amplitude of the position-dependent variance dipole, see Sect. 3.3 for details) between Gaussian CMB realizations including or not the local tSZ (at 143 GHz) and kSZ effects, when masking the galactic plane only (in red), and both the galactic plane and Virgo (in green). Distributions are shown for both the full set (solid lines) and the 5% (dashed) simulations where the hemispherical asymmetry is the strongest (largest A_d).

axis of asymmetry very close to the supergalactic plane, hinting at the local LSS as a possible explanation.

We have used the simulated maps of the tSZ and kSZ effects from the local Universe, together with Gaussian CMB realizations based on the *Planck* best fit cosmological parameters, to estimate the impact of these secondary anisotropies on the largest angular scales of the CMB fluctuations. Our analysis is based on the same estimators as for the analysis of large-scale anomalies in the *Planck* data, and we have shown that the local tSZ and kSZ effects cannot explain the detected deviations from isotropy.

Acknowledgements. We thank Adélie Gorce, Andrea Ravenni and Saleem Zaroubi for useful inputs and discussions. This work was supported by the grant agreements ANR-21-CE31-0019 / 490702358 from the French Agence Nationale de la Recherche / DFG for the LOCALIZATION project. NA acknowledges funding from the BvoPiC project from the European Research Council (ERC) under the European Union’s Horizon 2020 research and innovation program grant number ERC-2015-AdG 695561. KD acknowledges support by the COMPLEX project from the European Research Council (ERC) under the European Union’s Horizon 2020 research and innovation program grant agreement ERC-2019-AdG 882679. The authors acknowledge the Gauss Centre for Supercomputing e.V. (www.gauss-centre.eu) for funding this project by providing computing time on the GCS Supercomputer SuperMUC-NG at Leibniz Supercomputing Centre (www.lrz.de) under the projects pr86re, pr83li and pn68na. This research made use of observations obtained with *Planck* (<http://www.esa.int/Planck>), an ESA science mission with instruments and contributions directly funded by ESA Member States, NASA, and Canada. The authors acknowledge the use of the healpy and HEALPix packages (Zonca et al. 2019; Górski et al. 2005).

References

- Abdalla, E. et al. 2022, *JHEAp*, 34, 49
- Addison, G. E. 2024 [[arXiv:2403.10490](https://arxiv.org/abs/2403.10490)]
- Adhikari, S. 2015, *Mon. Not. Roy. Astron. Soc.*, 446, 4232
- Adhikari, S., Deutsch, A.-S., & Shandera, S. 2018, *Phys. Rev. D*, 98, 023520
- Adhikari, S., Shandera, S., & Erickcek, A. L. 2016, *Phys. Rev. D*, 93, 023524
- Aghanim, N., Majumdar, S., & Silk, J. 2008, *Rept. Prog. Phys.*, 71, 066902
- Agullo, I., Kranas, D., & Sreenath, V. 2021a, *Gen. Rel. Grav.*, 53, 17
- Agullo, I., Kranas, D., & Sreenath, V. 2021b, *Front. Astron. Space Sci.*, 8, 703845
- Akrami, Y., Fantaye, Y., Shafieloo, A., et al. 2014, *Astrophys. J. Lett.*, 784, L42
- Alonso, D., Sanchez, J., & Slosar, A. 2019, *Mon. Not. Roy. Astron. Soc.*, 484, 4127
- Amaro-Seoane, P., Audley, H., Babak, S., et al. 2017, *arXiv e-prints*, [arXiv:1702.00786](https://arxiv.org/abs/1702.00786)
- Ashoorioon, A. & Koivisto, T. 2016, *Phys. Rev. D*, 94, 043009

- Barausse, E., Berti, E., Hertog, T., et al. 2020, *General Relativity and Gravitation*, 52, 81
- Beck, A. M., Murante, G., Arth, A., et al. 2016, *MNRAS*, 455, 2110
- Bennett, C. L., Boggess, N. W., Cheng, E. S., et al. 1993, *Advances in Space Research*, 13, 409
- Bennett, C. L. et al. 2003, *Astrophys. J. Suppl.*, 148, 1
- Bertschinger, E. & Dekel, A. 1989, *ApJ*, 336, L5
- Billi, M., Barreiro, R. B., & Martínez-González, E. 2023 [arXiv:2312.09989]
- Billi, M., Gruppuso, A., Mandolesi, N., Moscardini, L., & Natoli, P. 2019, *Phys. Dark Univ.*, 26, 100327
- Blas, D., Lesgourgues, J., & Tram, T. 2011, *JCAP*, 07, 034
- Böhringer, H., Chon, G., & Trümper, J. 2021, *A&A*, 651, A15
- Bolliet, B., Hill, J. C., Ferraro, S., Kusiak, A., & Krolewski, A. 2023, *JCAP*, 03, 039
- Böss, L. M., Dolag, K., Steinwandel, U. P., et al. 2023 [arXiv:2310.13734]
- Byrnes, C. T., Regan, D., Seery, D., & Tarrant, E. R. M. 2016, *JCAP*, 06, 025
- Byrnes, C. T. & Tarrant, E. R. M. 2015, *JCAP*, 07, 007
- Chiocchetta, C., Gruppuso, A., Lattanzi, M., Natoli, P., & Pagano, L. 2021, *JCAP*, 08, 015
- Copi, C., Huterer, D., Schwarz, D., & Starkman, G. 2007, *Phys. Rev. D*, 75, 023507
- Copi, C. J., Huterer, D., Schwarz, D. J., & Starkman, G. D. 2006, *Mon. Not. Roy. Astron. Soc.*, 367, 79
- Copi, C. J., Huterer, D., Schwarz, D. J., & Starkman, G. D. 2009, *Mon. Not. Roy. Astron. Soc.*, 399, 295
- Copi, C. J., Huterer, D., Schwarz, D. J., & Starkman, G. D. 2015a, *Mon. Not. Roy. Astron. Soc.*, 451, 2978
- Copi, C. J., Huterer, D., Schwarz, D. J., & Starkman, G. D. 2015b, *Mon. Not. Roy. Astron. Soc.*, 449, 3458
- Copi, C. J., Huterer, D., & Starkman, G. D. 2004, *Phys. Rev. D*, 70, 043515
- Coulton, W. R., Feldman, S., Maamari, K., et al. 2022, *Mon. Not. Roy. Astron. Soc.*, 513, 2252
- Cruz, M., Martínez-González, E., Vielva, P., & Cayón, L. 2005, *MNRAS*, 356, 29
- Cruz, M., Tucci, M., Martínez-González, E., & Vielva, P. 2006, *MNRAS*, 369, 57
- Cruz, M., Vielva, P., Martínez-González, E., & Barreiro, R. B. 2011, *Mon. Not. Roy. Astron. Soc.*, 412, 2383
- de Oliveira-Costa, A., Tegmark, M., Zaldarriaga, M., & Hamilton, A. 2004, *Phys. Rev. D*, 69, 063516
- Dennis, M. R. 2004, *Journal of Physics A Mathematical General*, 37, 9487
- Dolag, K., Hansen, F. K., Roncarelli, M., & Moscardini, L. 2005, *Mon. Not. Roy. Astron. Soc.*, 363, 29
- Dolag, K., Komatsu, E., & Sunyaev, R. 2016, *Mon. Not. Roy. Astron. Soc.*, 463, 1797
- Dolag, K., Sorce, J. G., Pilipenko, S., et al. 2023, *Astron. Astrophys.*, 677, A169
- Douspis, M., Salvati, L., Gorce, A., & Aghanim, N. 2022, *Astron. Astrophys.*, 659, A99
- Dvorkin, C., Peiris, H. V., & Hu, W. 2008, *Phys. Rev. D*, 77, 063008
- Efstathiou, G. 2003, *Mon. Not. Roy. Astron. Soc.*, 346, L26
- Eriksen, H. K., Banday, A. J., Gorski, K. M., Hansen, F. K., & Lilje, P. B. 2007, *Astrophys. J. Lett.*, 660, L81
- Eriksen, H. K., Hansen, F. K., Banday, A. J., Gorski, K. M., & Lilje, P. B. 2004, *Astrophys. J.*, 605, 14, [Erratum: *Astrophys. J.* 609, 1198 (2004)]
- Eriksen, H. K., Jewell, J. B., Dickinson, C., et al. 2008, *Astrophys. J.*, 676, 10
- Fernandez-Cobos, R., Vielva, P., Barreiro, R. B., & Martínez-González, E. 2012, *Mon. Not. Roy. Astron. Soc.*, 420, 2162
- Fisher, K. B., Huchra, J. P., Strauss, M. A., et al. 1995, *ApJS*, 100, 69
- Galloni, G., Ballardini, M., Bartolo, N., et al. 2023, *JCAP*, 10, 013
- Galloni, G., Bartolo, N., Matarrese, S., et al. 2022, *JCAP*, 09, 046
- Gaztañaga, E. & Kumar, K. S. 2024 [arXiv:2401.08288]
- Jimeno-Amo, C., Barreiro, R. B., Matínez-González, E., & Marcos-Caballero, A. 2023 [arXiv:2306.14880]
- Górski, K. M., Hivon, E., Banday, A. J., et al. 2005, *ApJ*, 622, 759
- Groth, F., Steinwandel, U. P., Valentini, M., & Dolag, K. 2023, *MNRAS*, 526, 616
- Gruetjen, H. F., Fergusson, J. R., Liguori, M., & Shellard, E. P. S. 2017, *Phys. Rev. D*, 95, 043532
- Gruppuso, A. 2014, *Mon. Not. Roy. Astron. Soc.*, 437, 2076
- Gruppuso, A. & Gorski, K. M. 2010, *JCAP*, 03, 019
- Gruppuso, A., Natoli, P., Paci, F., et al. 2013, *JCAP*, 07, 047
- Hansen, F. K., Banday, A. J., Gorski, K. M., Eriksen, H. K., & Lilje, P. B. 2009, *Astrophys. J.*, 704, 1448
- Hansen, F. K., Boero, E. F., Luparello, H. E., & Lambas, D. G. 2023, *Astron. Astrophys.*, 675, L7
- Hansen, F. K., Gorski, K. M., & Hivon, E. 2002, *Mon. Not. Roy. Astron. Soc.*, 336, 1304
- Hansen, F. K., Trombetti, T., Bartolo, N., et al. 2019, *Astron. Astrophys.*, 626, A13
- Hernández-Martínez, E., Dolag, K., Seidel, B., et al. 2024 [arXiv:2402.01834]
- Heß, S., Kitaura, F.-S., & Gottlöber, S. 2013, *MNRAS*, 435, 2065
- Hill, J. C. & Pajer, E. 2013, *Phys. Rev. D*, 88, 063526
- Hinshaw, G., Banday, A. J., Bennett, C. L., et al. 1996, *Astrophys. J. Lett.*, 464, L25
- Hirschmann, M., Dolag, K., Saro, A., et al. 2014, *Mon. Not. Roy. Astron. Soc.*, 442, 2304
- Hivon, E., Gorski, K. M., Netterfield, C. B., et al. 2002, *Astrophys. J.*, 567, 2
- Hoftuft, J., Eriksen, H. K., Banday, A. J., et al. 2009, *Astrophys. J.*, 699, 985
- Jasche, J. & Wandelt, B. D. 2013, *MNRAS*, 432, 894
- Jazayeri, S., Sadr, A. V., & Firouzjahi, H. 2017, *Phys. Rev. D*, 96, 023512
- Jones, J., Copi, C. J., Starkman, G. D., & Akrami, Y. 2023 [arXiv:2310.12859]
- Jung, G., Oppizzi, F., Ravenni, A., & Liguori, M. 2020, *JCAP*, 06, 035
- Karachentsev, I. D. & Telikova, K. N. 2018, *Astron. Nachr.*, 339, 615
- Kester, C. E., Bernui, A., & Hipólito-Ricaldi, W. S. 2023 [arXiv:2310.02928]
- Kitaura, F. S. & Enßlin, T. A. 2008, *MNRAS*, 389, 497
- Kravtsov, A. V., Klypin, A. A., & Hoffman, Y. 2002, *Astrophys. J.*, 571, 563
- Kumar, K. S. & Marto, J. a. 2022 [arXiv:2209.03928]
- Lambas, D. G., Hansen, F. K., Toscano, F., Luparello, H. E., & Boero, E. F. 2024, *Astron. Astrophys.*, 681, A2
- Land, K. & Magueijo, J. 2005, *Phys. Rev. Lett.*, 95, 071301
- Lavaux, G. 2010, *MNRAS*, 406, 1007
- Luparello, H. E., Boero, E. F., Lares, M., Sánchez, A. G., & Lambas, D. G. 2022, *Mon. Not. Roy. Astron. Soc.*, 518, 5643
- Marcos-Caballero, A. & Martínez-González, E. 2019, *JCAP*, 10, 053
- Marcos-Caballero, A., Martínez-González, E., & Vielva, P. 2017, *JCAP*, 05, 023
- Mathis, H., Lemson, G., Springel, V., et al. 2002, *MNRAS*, 333, 739
- Maxwell, J. C. 1865, *Phil. Trans. Roy. Soc. Lond.*, 155, 459
- McAlpine, S., Helly, J. C., Schaller, M., et al. 2022, *Mon. Not. Roy. Astron. Soc.*, 512, 5823
- Monteserin, C., Barreiro, R. B. B., Vielva, P., et al. 2008, *Mon. Not. Roy. Astron. Soc.*, 387, 209
- Muir, J., Adhikari, S., & Huterer, D. 2018, *Phys. Rev. D*, 98, 023521
- Natale, U., Gruppuso, A., Molinari, D., & Natoli, P. 2019, *JCAP*, 12, 052
- Oliveira, R. A., Pereira, T. S., & Quartin, M. 2020, *Phys. Dark Univ.*, 30, 100608
- Patel, S. K., Aluri, P. K., & Ralston, J. P. 2024 [arXiv:2405.03024]
- Planck Collaboration. 2014a, *A&A*, 571, A16
- Planck Collaboration. 2014b, *A&A*, 571, A23
- Planck Collaboration. 2016a, *A&A*, 594, A16
- Planck Collaboration. 2016b, *A&A*, 596, A101
- Planck Collaboration. 2020a, *A&A*, 641, A7
- Planck Collaboration. 2020b, *A&A*, 643, A42
- Salvati, L., Douspis, M., & Aghanim, N. 2018, *Astron. Astrophys.*, 614, A13
- Schmidt, F. & Hui, L. 2013, *Phys. Rev. Lett.*, 110, 011301, [Erratum: *Phys. Rev. Lett.* 110, 059902 (2013)]
- Schwarz, D. J., Copi, C. J., Huterer, D., & Starkman, G. D. 2016, *Class. Quant. Grav.*, 33, 184001
- Schwarz, D. J., Starkman, G. D., Huterer, D., & Copi, C. J. 2004, *Phys. Rev. Lett.*, 93, 221301
- Scodeller, S., Rudjord, O., Hansen, F. K., et al. 2011, *Astrophys. J.*, 733, 121
- Shi, R. et al. 2023, *Astrophys. J.*, 945, 79
- Sorce, J. G. 2018, *Mon. Not. Roy. Astron. Soc.*, 478, 5199
- Sorce, J. G., Courtois, H. M., Gottlöber, S., Hoffman, Y., & Tully, R. B. 2014, *Mon. Not. Roy. Astron. Soc.*, 437, 3586
- Sorce, J. G., Gottlöber, S., Yepes, G., et al. 2016, *Mon. Not. Roy. Astron. Soc.*, 455, 2078
- Spergel, D. N. et al. 2003, *Astrophys. J. Suppl.*, 148, 175
- Springel, V. 2005, *Mon. Not. Roy. Astron. Soc.*, 364, 1105
- Sunyaev, R. A. & Zeldovich, Y. B. 1972, *Comments Astrophys. Space Phys.*, 4, 173
- Sunyaev, R. A. & Zeldovich, Y. B. 1980a, *Ann. Rev. Astron. Astrophys.*, 18, 537
- Sunyaev, R. A. & Zeldovich, Y. B. 1980b, *Mon. Not. Roy. Astron. Soc.*, 190, 413
- Suzuki, A., Ade, P. A. R., Akiba, Y., et al. 2018, *Journal of Low Temperature Physics*, 193, 1048
- Tristram, M., Macías-Pérez, J. F., Renault, C., & Santos, D. 2005, *Mon. Not. Roy. Astron. Soc.*, 358, 833
- Tully, R. B. et al. 2013, *Astron. J.*, 146, 86
- Vielva, P. 2010, *Advances in Astronomy*, 2010, 592094
- Vielva, P., Martínez-González, E., Barreiro, R. B., Sanz, J. L., & Cayón, L. 2004, *ApJ*, 609, 22
- Vogelsberger, M., Marinacci, F., Torrey, P., & Puchwein, E. 2020, *Nature Rev. Phys.*, 2, 42
- Wandelt, B. D., Hivon, E., & Gorski, K. M. 1998 [arXiv:astro-ph/9808292]
- Wang, H., Mo, H. J., Yang, X., & van den Bosch, F. C. 2013, *ApJ*, 772, 63
- Whitbourn, J. R. & Shanks, T. 2014, *Mon. Not. Roy. Astron. Soc.*, 437, 2146
- Yang, Q., Yu, H., & Di, H. 2019, *Phys. Dark Univ.*, 26, 100407
- Zeldovich, Y. B. & Sunyaev, R. A. 1969, *Astrophys. Space Sci.*, 4, 301
- Zonca, A., Singer, L., Lenz, D., et al. 2019, *Journal of Open Source Software*, 4, 1298

Appendix A: The *Planck* position-dependent power spectrum

In addition to the position-dependent variance, skewness and kurtosis analyses presented in Sect. 3.3, we consider the position-dependent power spectrum. When used up to small scales where noise becomes dominant, it has been shown to be an efficient ingredient to study several signatures of non-Gaussianity, like the primordial local template or the correlations between the ISW and lensing effects (see Jung et al. 2020, and references therein). Here, in the spirit of this paper, we focus only on large angular scales ($\ell \leq 50$), and the rest will be included in a future work.

For this analysis, we use a set of patches based on Mexican needlets (see Scodeller et al. 2011, for details), which have the advantage of having simple expressions in harmonic space, but are not exactly localized in real space, unlike the discs and pixels. A needlet patch map centered at the position Ω_c is obtained using,

$$M_{p,B,j}^{\text{patch}}(\Omega; \Omega_c) = \sum_{\ell} \frac{2\ell + 1}{4\pi} \left[\frac{\ell(\ell + 1)}{B^{2j}} \right]^p e^{-\frac{\ell(\ell+1)}{B^{2j}}} P_{\ell}(\Omega \cdot \Omega_c), \quad (\text{A.1})$$

where P_{ℓ} is a Legendre polynomial and, p , B and j are the needlet parameters. Here we use the values $p = 1$, $b = 4$ and $j = 1$, for which only terms with $\ell \leq 10$ are sufficient to compute the sum, and 192 patches are enough to cover uniformly the full sky. In Fig. A.1, we show an example of such needlet patch, along with the pixels and discs used in sections 3.3 and B, respectively.

As in Sect. 4.1, we measure pseudo- C_{ℓ} up to $\ell_{\text{max}} = 50$, using NaMaster in each of the 192 needlet patches defined above. For each multipole of the position-dependent power spectrum, we measure a dipole (following the same pipeline as for the position-dependent variance). All the corresponding directions are shown in Fig. A.2. An important result is that all the dipoles are localized in less than half the sky, as they point in both the southern ecliptic and supergalactic hemispheres (at the exception of $\ell = 47$, slightly over the ecliptic plane), and the angular difference between close multipoles is almost always small, indicating some correlation between them. However, opposed to the variance case, the amplitude of the data dipoles is in the expected range obtained from the simulations, meaning this estimator is not sensitive to the hemispherical asymmetry.

In Fig. A.3, we compare the observed position-dependent power spectrum to the distribution determined from the corresponding simulations. On the largest scales ($\ell = 2, 3$ and 4), the observed value is close to the 5% lowest simulations, which is related to the lack-of-power/lack-of-correlation anomaly. When repeating the same analysis on half the sky, using the dipole directions determined above, we find that the hemisphere opposed to the dipole has a low power up to $\ell = 7$, and is among the 1-2% range on the largest scales. However, the other hemisphere also has a relatively low power at low multipoles (20% lowest simulations).

Appendix B: The *Planck* position-dependent variance with discs

Here, we report the main results of our analysis of the position-dependent variance of the *Planck* PR4 CMB temperature maps, where we use discs of 4° radius as patches.

The conclusions from Figs. B.1 and B.2 are very similar to the ones reported in Sect. 3.3 with the HEALPix pixel patches.

The large dipole of the observed position-dependent variance confirms the presence of a strong hemispherical asymmetry, maximized when separating the sky close to the supergalactic plane, with a significant lack of variance in the northern half. Note that with the disc patches, this anomaly is stronger than in any of the simulations. For further analyses of the hemispherical asymmetry in the PR4 data, including polarization, with the same disc patches, we refer the reader to Gimeno-Amo et al. (2023).

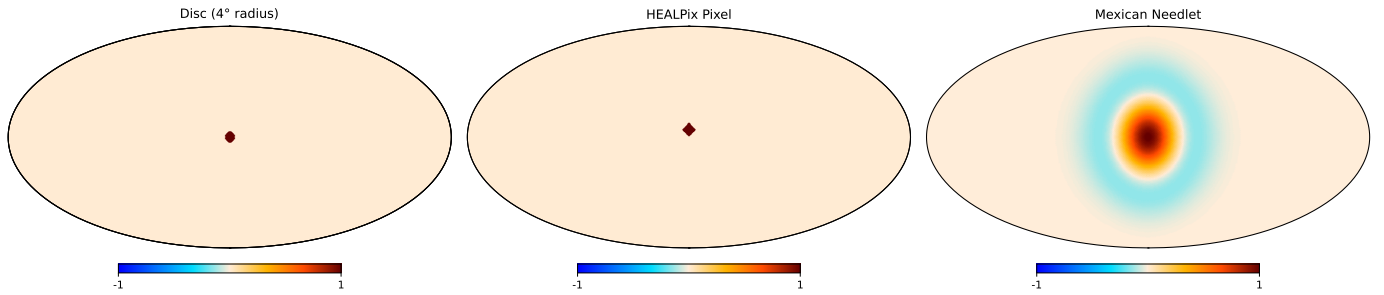


Fig. A.1. Maps of the disc, HEALPix pixel and Mexican needlet patches used in this work to evaluate position-dependent statistics. The three complete sets include 3072 4° radius discs, 768 pixels (corresponding to the pixels of a $N_{\text{side}} = 8$ HEALPix map) and 192 Mexican needlets ($p = 1$, $b = 4$ and $j = 1$). Note that all patches have been set to 1 at their center in this figure.

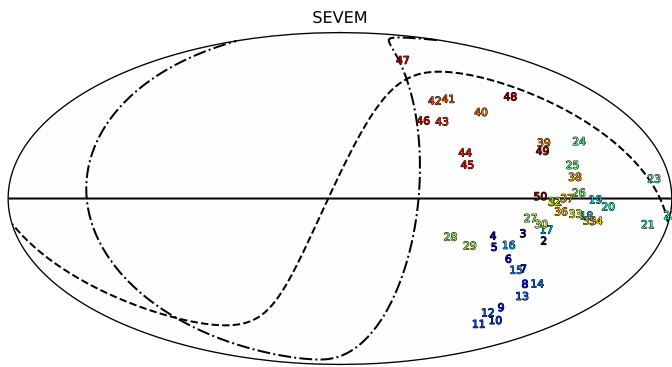


Fig. A.2. Dipole directions of the position-dependent power spectrum in the *Planck* PR4 SEVEM map (Commander results being very similar), for each multipole up to $\ell = 50$. The black solid, dashed and dash-dotted lines correspond to the galactic, ecliptic and supergalactic planes, respectively.

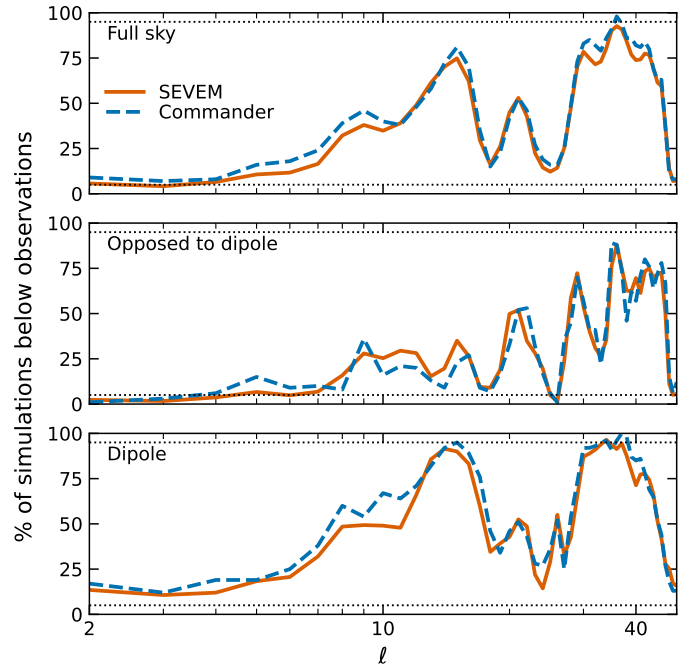


Fig. A.3. Comparison between the position-dependent power spectrum in the *Planck* PR4 CMB temperature data and simulated maps. We average the position-dependent power spectrum over the full sky (upper panel), and the two hemispheres defined by the dipole of each multipole (opposed to dipole in the middle panel and dipole direction otherwise), and compare the observed value to the equivalent from the simulations. We show the percentage of simulations having a lower value than the data. Horizontal black dotted lines indicate the 5% and 95% thresholds.

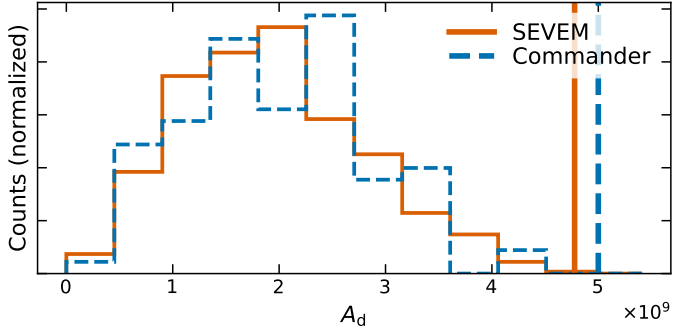


Fig. B.1. Distribution of the amplitude of the position-dependent variance dipole (using discs of 4° radius) in the *Planck* PR4 CMB temperature data illustrating the hemispherical asymmetry anomaly. The orange and blue vertical lines correspond to the observed SEVEM and Commander maps, respectively, and the histograms are obtained from the corresponding 600 SEVEM (orange), and 100 Commander (blue) simulations. None of the simulated CMB maps have a large dipole amplitude value.

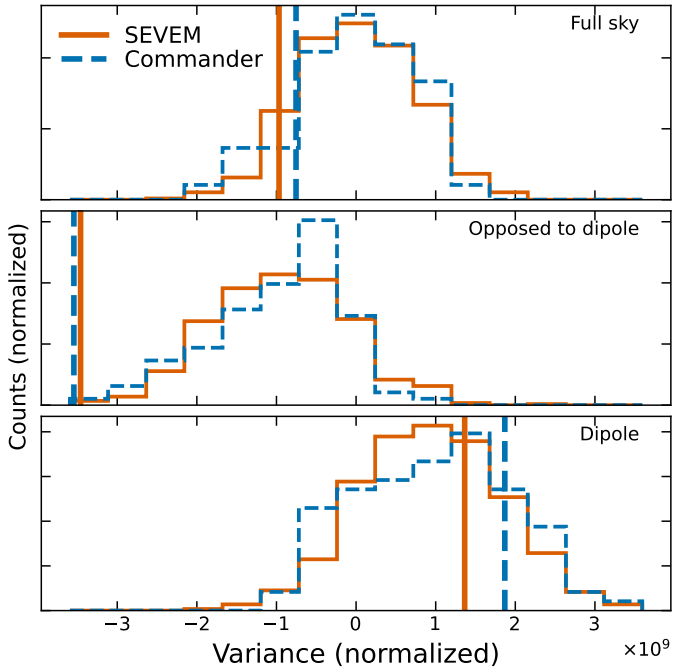


Fig. B.2. Similar to Fig. 7, for the position-dependent variance computed with discs of 4° radius as patches. None of the simulated CMB maps have a lower averaged position-dependent variance in the direction opposed to their respective dipoles than the observations (close to the northern supergalactic hemisphere).